11 May 2026

Sulfur-Induced Lattice Disordering in Halide Electrolytes Enables Superionic Sodium Ion Conduction

Feng Jin[1,2], Bingxu Wang[1], Meenal Agrawal[2], Ingeborg Sellæg Ellingsen[2], Guobiao Jin[1], Lulu Alluhaibi[3], Alexey Maximenko[3], Marcin Zając[3], Dragos Stoian[4], Kenneth Marshall[4], Wouter Van Beek[4], Feng Pan[1], Daniel Rettenwander[2,5,6]

1. School of Advanced Materials, Peking University Shenzhen Graduate School
2. Department of Material Science and Engineering, NTNU Norwegian University of Science and Technology
3. Jagiellonian University
4. European Synchrotron Radiation Facility
5. Christian Doppler Laboratory for Solid-State Batteries, NTNU Norwegian University of Science and Technology
6. Institute of Chemical Technologies and Analytics, Vienna University of Technology

Abstract

Amorphous solid electrolytes provide a promising route to overcome the ion-transport limitations of crystalline halide frameworks, yet achieving superionic Na+ conduction remains challenging. Herein, we report a mixed-anion amorphous Na-ion solid-state electrolyte, TaCl5-0.5Na2S (NTSC), synthesized via high-energy ball milling, which exhibits an ultrahigh room-temperature ionic conductivity of 2.9 mS/cm and a low activation energy of 0.276 eV. Structural analyses reveal a highly disordered framework composed of Ta-centered bi-polyhedral interconnected via corner-sharing sulfur atoms [Ta2Cl10S], evidenced by comprehensive characterizations, forming a flexible, disordered amorphous network. Ab initio molecular dynamics simulations identify continuous Na + diffusion pathways with low migration barriers. Complementary topological analyses further indicate that sulfur incorporation leads to local lattice distortions, shortens Na-Na hopping distances, and enhances framework flexibility, collectively enabling fast, multidimensional Na + transport. When applied in all-solid-state sodium-ion batteries, NTSC enables high reversible capacity (111.95 mAh/g with a Coulombic efficiency of 92.6 % at 0.1 C) and excellent cycling stability (76.9 % initial capacity retention after 200 cycles at 0.2 C) at room temperature. This work establishes mixed-anion amorphization as an effective design strategy for high-performance Na-ion solid electrolytes.

Sulfur-Induced Lattice Disordering in Halide Electrolytes Enables Superionic Sodium Ion Conduction

Feng Jin[1,2†], Bingxu Wang[1†], Meenal Agrawal[2], Ingeborg Sellæg Ellingsen[2], Guobiao Jin[1], Lulu Alluhaibi[3], Alexey Maximenko[3], Marcin Zając[3], Dragos Stoian[4], Kenneth Marshall[4], Wouter Van Beek[4], Feng Pan[1], Daniel Rettenwander[2,5-7**]*

[1]School of Advanced Materials, Peking University Shenzhen Graduate School, Shenzhen, 518055, China
[2]Department of Material Science and Engineering, NTNU Norwegian University of Science and Technology, Trondheim 7491, Norway
[3]National Synchrotron Radiation Centre SOLARIS, Jagiellonian University, Czerwone Maki 98, 30-392, Kraków, Poland
[4]Swiss-Norwegian Beamlines, European Synchrotron Radiation Facility, 71 Ave. des Martyrs, Grenoble 38000, France
[5]Christian Doppler Laboratory for Solid-State Batteries, NTNU Norwegian University of Science and Technology, Trondheim 7491, Norway
[6]AIT Austrian Institute of Technology GmbH, Giefinggasse 2, Vienna, 1210, Austria.
[7]Institute of Chemical Technologies and Analytics, Vienna University of Technology, Getreidemarkt 9, Vienna, 1060, Austria.

[†]Feng Jin and Bingxu Wang contributed equally to this work.

Corresponding authors: [*]panfeng@pkusz.edu.cn, [**]daniel.rettenwander@ntnu.no

Abstract

Amorphous solid electrolytes provide a promising route to overcome the ion-transport limitations of crystalline halide frameworks, yet achieving superionic Na^+ conduction remains challenging. Herein, we report a mixed-anion amorphous Na-ion solid-state electrolyte, $TaCl_5$-$0.5Na_2S$ (NTSC), synthesized via high-energy ball milling, which exhibits an ultrahigh room-temperature ionic conductivity of 2.9 mS/cm and a low activation energy of 0.276 eV. Structural analyses reveal a highly disordered framework composed of Ta-centered bi-polyhedral interconnected via corner-sharing sulfur atoms [$Ta_2Cl_{10}S$], evidenced by comprehensive characterizations, forming a flexible, disordered amorphous network. *Ab initio* molecular dynamics simulations identify continuous Na^+ diffusion pathways with low migration barriers. Complementary topological analyses further indicate that sulfur incorporation leads to local lattice distortions, shortens Na-Na hopping distances, and enhances framework flexibility, collectively enabling fast, multidimensional Na^+ transport. When applied in all-solid-state sodium-ion batteries, NTSC enables high reversible capacity (111.95 mAh/g with a Coulombic efficiency of 92.6 % at 0.1 C) and excellent cycling stability (76.9 % initial capacity retention after 200 cycles at 0.2 C) at room temperature. This work establishes mixed-anion amorphization as an effective design strategy for high-performance Na-ion solid electrolytes.

Introduction

All-solid-state sodium-ion batteries (ASSNIBs) have emerged as promising candidates for grid-scale energy storage and cost-sensitive electric mobility applications, owing to the natural abundance, low cost, and environmental benignity of sodium, together with the intrinsic safety advantages afforded by solid electrolytes[1]. A critical challenge in realizing high-performance ASSNIBs is the development of Na-ion solid-state electrolytes (Na-SSEs) that simultaneously deliver high ionic conductivity (> 0.1 mS/cm at room temperature), negligible electronic conductivity, and robust electrochemical, chemical, and mechanical compatibility with both cathode and anode materials[2].

Over the past decades, a wide range of Na-SSEs has been explored, including oxide-based NASICON-type conductors ($Na_{1+x}Zr_2Si_xP_{3-x}O_{12}$), sulfide electrolytes (e.g., Na_3PS_4 and Na_3SbS_4), and halide-based systems (e.g., Na_3YCl_6 and Na_2ZrCl_6)[3,4]. Among these material classes, chloride-based Na-SSEs have attracted increasing attention due to their wide electrochemical stability windows, high oxidation resistance, and favorable mechanical properties and processability[5]. However, their practical deployment remains constrained by intrinsically limited Na^+ conductivity, which originates from close-packed halide lattices, rigid anion frameworks, and fixed Na^+ coordination geometries. To mitigate these limitations, aliovalent cation doping strategies—such as substitution with Er^{3+} and other rare-earth cations—have been employed to introduce Na^+ vacancies and lattice disorder, yielding conductivities exceeding 0.1 mS/cm at room temperature[6]. Despite these advances, further enhancement of Na^+ transport is essential for competitive ASSNIB performance.

In parallel, amorphous solid electrolytes have gained increasing interest as alternatives to crystalline counterparts, as the absence of long-range order eliminates grain-boundary resistance and relaxes crystallographic constraints on ion migration. The resulting structural and energetic disorder enables isotropic Na^+ transport through a heterogeneous energy landscape and allows dynamic local structural relaxation during ion hopping. To date, extensive efforts have focused on oxide-based glassy Na-SSEs (e.g., Na_2O-P_2O_5, Na_2O-B_2O_3, and Na_2O-SiO_2) and sulfide-based systems (e.g., Na_2S-P_2S_5-SiS_2, Na_3PS_4-Na_4GeS_4, Na_2S-P_2S_5 and Na_2S-B_2S_3)[7–9]. In these materials, Na^+ migration occurs through disordered anion networks composed of motifs such as S^{2-}, PS_4^{3-}, and $P_2S_7^{4-}$ units. Nevertheless, strong coulombic interactions, limited framework flexibility, and non-ideal Na^+ coordination environments often lead to insufficient room-temperature ionic conductivities, thereby hindering their widespread implementation in ASSNIB architectures.

More recently, amorphous chloride-based Na-SSEs have emerged as a compelling new materials platform, exhibiting room-temperature ionic conductivities exceeding 1 mS/cm. Representative systems, including $NaTaCl_6$-derived glasses and mixed-anion compositions such as Na_2O_2-$TaCl_5$ and Na_2CO_3-$TaCl_5$, demonstrate that the incorporation of multiple anionic species fundamentally reshapes the local structural

and electrostatic landscape[10–12]. Mixed-anion frameworks introduce pronounced structural disorder, weaken Na^+-anion interactions, and generate a broad distribution of Na^+ coordination environments, collectively flattening the migration energy landscape and enabling rapid ion transport[11]. These advances highlight the critical role of anion chemistry and amorphization in overcoming the intrinsic conductivity limitations of crystalline halide electrolytes and opening new avenues for the rational design of high-performance Na-SSEs.

Herein, we report a new amorphous superionic Na-SSE, $TaCl_5$-0.5Na_2S (NTSC), synthesized via high-energy ball milling using $TaCl_5$ and Na_2S as precursors. The resulting amorphous NTSC matrix consists primarily of Ta-centered bi-polyhedral interconnected via corner-sharing sulfur atoms [$Ta_2Cl_{10}S$], proved by multiple characterizations, including Raman spectroscopy, X-ray photoelectron spectroscopy (XPS), X-ray absorption spectroscopy (XAS) and X-ray pair distribution function (xPDF) analysis. This distinctive mixed-anion local structure weakens Na^+-lattice interactions and promotes a flexible, disordered framework, facilitating rapid long-range Na^+ transport and yielding a high ionic conductivity of 2.9 mS/cm at 25 °C. *Ab initio* molecular dynamics simulations reveal continuous Na^+ diffusion pathways with low migration barriers, consistent with the experimentally observed superionic behavior. Complementary topological analyses further indicate that sulfur incorporation induces local lattice distortions, shortens Na-Na hopping distances, and enhances framework flexibility, collectively enabling fast, multidimensional Na^+ transport. When paired with an uncoated $NaCrO_2$ cathode, NTSC-based ASSNIBs deliver a high initial discharge capacity of 111.95 mAh/g with a Coulombic efficiency of 92.6 % and retain 76.9 % of their capacity after 200 cycles at 0.2 C and 25 °C. This work introduces a new class of amorphous mixed-anion Na-SSEs, demonstrates their effectiveness in enabling high-performance ASSNIBs, and provides design principles for the future development of amorphous halide electrolytes.

Results and Discussions

A series of amorphous solid electrolytes with nominal compositions $TaCl_5$-$x$$Na_2S$ (x = 0.25, 0.5, 0.75, and 1.0), namely $TaCl_5$-$x$$Na_2S$, were synthesized via high-energy ball milling using $TaCl_5$ and Na_2S as precursors (Figure 1a). High-energy mechanical processing promotes intimate mixing and solid-state reactions between the precursors while suppressing long-range crystallization.

The degree of amorphization was evaluated by X-ray diffraction (XRD), as the absence of sharp Bragg reflections is indicative of a glassy or amorphous structure. The corresponding XRD patterns are shown in Figure 1c. Systematic optimization of the precursor stoichiometry reveals that a fully amorphous phase is obtained at x = 0.5, as evidenced by the presence of broad diffraction halos and the complete absence of crystalline peaks (see also Figure S2). In contrast, samples with higher Na_2S content (x = 0.75 and 1.0) exhibit the emergence of distinct diffraction peaks, which can be unambiguously assigned to crystalline

NaCl and residual Na_2S phases, indicating phase separation and incomplete amorphization at elevated *x* values[11,13].

Accordingly, the thermal properties of the optimized $TaCl_5$-0.5Na_2S composition (denoted as NTSC) were examined by differential scanning calorimetry (DSC). The DSC trace (Figure S4) exhibited a clear glass transition at 193 °C without any detectable crystallization exotherms upon heating, indicating a stable glass framework with moderate network rigidity, which is favorable for maintaining dynamic local environments that support Na^+ migration.

The Na^+ ionic conductivities of the $TaCl_5$-*x*Na_2S series were evaluated by electrochemical impedance spectroscopy (EIS) over a temperature range of 25-70 °C. Representative Nyquist plots of NTSC display a depressed semicircle in the high-frequency region, corresponding to bulk ionic transport, followed by a low-frequency spike associated with ion-blocking electrodes (Figure 1d, Figure S5). Based on EIS fitting (deteails in experimental section), the optimized amorphous NTSC electrolyte delivered a room-temperature ionic conductivity of up 2.9 mS/cm at 25 °C (Figure 1e). The Arrhenius behavior of the Na-ion conductivity for all compositions (Figure 1f) in the temperature range between 25 °C and 70 °C has been studies for all compositions. The corresponding activation energy is as low as 0.276 eV, highlighting its exceptionally favorable ion-transport kinetics. To benchmark its performance, the room-temperature ionic conductivity of NTSC is compared with those of representative inorganic Na-SSEs reported in the literature. As summarized in Table S1, NTSC outperforms most reported Na-SSEs, while some recently reported mixed-anion systems (e.g., NTOC) exhibiting comparable ionic conductivities (4.62 mS/cm) and activation energy (0.30 eV)[11].

To elucidate the structural features of amorphous NTSC, a combination of complementary characterization techniques sensitive to short-range atomic order was employed, including Raman spectroscopy, XPS, XAS and xPDF analysis. Given its superior ionic conductivity and representative structural features, detailed characterization was focused on the optimized $TaCl_5$-0.5Na_2S composition.

Raman spectroscopy provides direct insight into local bonding environments and coordination motifs in amorphous materials. The Raman spectrum (Figure 2a) of NTSC exhibits a broad, featureless profile compared to the sharp and well-defined vibrational modes of the crystalline $TaCl_5$ and Na_2S precursors, consistent with the formation of a highly disordered amorphous structure. The characteristic vibrational signatures of $TaCl_5$ and Na_2S are largely suppressed or significantly broadened in NTSC, indicating substantial disruption of long-range periodicity. Notably, broad bands appearing in the 150-350 cm^{-1} and 300-400 cm^{-1} regions can be attributed to Ta-centered polyhedral vibrations coupled with sulfur coordination, suggesting the formation of corner-sharing [$Ta_2Cl_{10}S$] oligomeric units within the amorphous matrix[14,15]. Sulfur bridging is further evidenced by Ta 4f X-ray photoelectron spectroscopy (XPS) spectrum with extra peaks locating at around 27 eV and 29 eV (Figure 2b).

Complementary to Raman spectroscopy and XPS, which is sensitive to local vibrational environments and chemical bonding, X-ray absorption spectroscopy (XAS) offers element-specific information on local coordination geometry and electronic structure. The normalized S *K-edge* X-ray absorption near-edge structure (XANES) spectrum of NTSC exhibits two shoulder features at around 2471.1 and 2473.4 eV, coinciding with those of Na_2S, indicating a similar sulfur oxidation state (Figure 2c)[16]. In addition, two distinct features at around 2469.0 and 2472.2 eV are observed, which can be attributed to Ta-S interactions, suggesting that the S 1s → p/d hybridized transitions in NTSC are influenced by coordination with Ta^{5+} rather than solely by Na^+. The Na *K-edge* XANES spectra of NTSC and Na_2S (Figure S6) show close correspondence in both peak positions and line shapes, indicating that the local chemical environment of Na^+ remains largely unchanged upon amorphization, consistent with its role as a weakly coordinated, mobile charge carrier. Similarly, the Cl *K-edge* XANES spectrum of NTSC exhibits no pronounced peak shifts or line-shape changes relative to the $TaCl_5$ precursor (Figure S7), suggesting that Cl retains a comparable local coordination environment in the amorphous state.

Furthermore, the Ta L_3*-edge* XANES and corresponding Fourier Transform -EXAFS reveal systematic modifications of the local electronic and structural environment upon S incorporation into the $TaCl_5$-derived material. In $TaCl_5$, Ta^{5+} ($5d^0$) is coordinated by six Cl atoms forming distorted edge-sharing $TaCl_6$ octahedra, with Ta-Cl bond lengths ranging from 2.26 to 2.56 Å. The XANES spectrum of such a distorted octahedral structure shows a broad peak with an indistinct top at the white-line position. Moreover, the structural distortion of the octahedral symmetry generally leads to a small splitting of the 5d states as can be precisely seen in the second derivative plot displaying two minima (ca. 2.8 eV split in $TaCl_5$) (Figure S8). Upon S incorporation, white-line intensity of NTSC decreases without a noticeable edge shift, indicating that Ta largely retains its pristine +5 oxidation state while exhibiting reduced unoccupied 5d density of states, consistent with enhanced metal-ligand covalency due to the more covalent nature of S relative to Cl. The post-edge region (~9890-9900 eV) becomes slightly damp, suggesting increased structural disorder (Figure 2d). The second-derivative spectrum shows broadened features and a modest increase in apparent splitting (~0.4 eV), indicative of mixed Ta-Cl/S coordination environments (Figure S8). Fourier Transform-EXAFS analysis shows that the first-shell peak shifts to higher radial distance (from 1.89 Å in $TaCl_5$ to 1.96 Å in NTSC, uncorrected for phase shift), accompanied by peak broadening and reduced amplitude, reflecting an increase in average Ta-ligand bond length and greater structural heterogeneity, consistent with partial substitution of Cl by larger, less electronegative S atoms (typical Ta-S ≈ 2.47 Å, obtained from crystallographic databases) (Figure 2e). The observed broadening and amplitude reduction of the first-shell peak of the sample suggests a distribution of local environments arising from mixed Ta-Cl and Ta-S coordination and increased disorder. Wavelet Transform-EXAFS further supports increased disorder, as evidenced by faster k-space damping at high k for NTSC. In contrast, the higher-R region (3-5 Å) remains

largely preserved (Figure 2f & 2g). Together, these results support a scenario in which S incorporation induces local structural and electronic perturbations - manifested as elongated and more heterogeneous Ta-ligand bonding - while maintaining the overall TaCl5-derived structural motif.

While EXAFS primarily probes the local coordination environment around a selected absorber, xPDF analysis provides real-space information on both short- and medium-range atomic correlations, independent of long-range periodicity, making it particularly effective for probing amorphous structures. The xPDF of $TaCl_5$, $NaTaCl_6$ (NTC), and NTSC reveals that in the first coordination shell, two distinct Ta-Cl peaks at 2.23 and 2.58 Å merge in $TaCl_5$, while in NTC the bridging Ta-Cl feature disappears due to isolated [$TaCl_6$] octahedra, with the main Ta-Cl peak shifting to 2.30 Å. Partial substitution of Cl by S further shifts this peak to 2.32 Å, reflecting the longer Ta-S bond lengths relative to Ta-Cl. In the second coordination shell, the Ta-Ta peak at 3.85 Å in $TaCl_5$ vanishes in NTC, consistent with octahedral isolation, but reappears at 3.69 Å in NTSC, arising from corner-sharing [$Ta_2Cl_{10}S$] octahedra (Figure 2h). These results demonstrate how local and medium-range structural motifs evolve upon Cl substitution and octahedral connectivity changes, highlighting the sensitivity of xPDF to both bond-length variations and coordination topology.[11].

To gain atomic-scale insight into the origin of the experimentally observed superionic Na^+ transport in NTSC, *ab initio* molecular dynamics (AIMD) simulations were performed. These simulations were designed to directly interrogate Na^+ migration pathways, diffusion kinetics, and their structural origins in the amorphous mixed-anion framework.

As shown in Figure 3a, the simulated Na^+ trajectories in NTSC reveal continuous and percolating diffusion pathways extending across the simulation cell, indicating a structurally connected environment that supports long-range Na^+ transport. This observation is consistent with the experimentally inferred cavity-rich amorphous framework and the Ta-centered oligomeric connectivity identified by Raman, XAS, and PDF analyses. The temperature-dependent Na^+ diffusion coefficients extracted from AIMD exhibit excellent Arrhenius behavior (Figure S9b), confirming the internal consistency of the simulations and enabling quantitative comparison with experimental transport measurements. Quantitatively, the Na-ion diffusion coefficients obtained from AIMD are 1.34×10^{-5}, 2.53×10^{-5}, 3.09×10^{-5}, and 5.16×10^{-5} $cm^2\ s^{-1}$ at 600, 800, 1000, and 1200 K, respectively. Fitting this data yields an activation energy of 0.130 eV, indicative of a low energetic barrier for Na-ion hopping. This close correspondence validates the AIMD model and confirms that the low migration barrier observed experimentally originates from intrinsic features of the amorphous NTSC framework rather than extrinsic effects. Extrapolation to room temperature gives a Na^+ diffusion coefficient of 1.06×10^{-6} $cm^2\ s^{-1}$ and a corresponding ionic conductivity of 9.31×10^{-3} S/ cm at 300 K, collectively highlighting the intrinsically fast-ion-conducting nature of NTSC and supporting its potential as a high-performance Na-ion conductor. To isolate the structural factors responsible for the enhanced Na^+ mobility, a comparative analysis was carried out against crystalline NTC,

a structurally related but transport-limited halide reference. While both systems exhibit comparable Na^+ transport channels and pore geometries (Figures S7a), the incorporation of sulfur in NTSC induces pronounced distortions of the Ta-centered coordination environment. These distortions shorten the Na-Na hopping distances from 5.13 Å in NTC to 4.46-4.91 Å in NTSC, directly reducing the energetic penalty for Na^+ hopping and facilitating more frequent site-to-site migration. Radial distribution function analyses further reveal that Na^+ coordination in NTC is dominated by relatively rigid Na-Cl interactions, whereas in NTSC these interactions are largely replaced by Na-S coordination. Because S^{2-} is more polarizable and forms a softer electrostatic environment than Cl^-, the resulting energy landscape experienced by migrating Na^+ ions is significantly flattened, consistent with the experimentally observed reduction in activation energy.

While conventional analyses focus primarily on identifying dominant migration pathways, such approaches capture only limited zero-dimensional structural information. To achieve a more comprehensive understanding of how the amorphous framework topology governs ion transport, topological data analysis was employed to probe higher-dimensional connectivity features. As shown in Figures 3e and 3f, topological invariants were computed for both the Na^+ subnetwork and the non-Na framework in NTSC and NTC. In the Na^+ subnetwork, the zero-dimensional Betti-number barcodes of NTSC terminate sharply within the 4.0-5.0 Å range, indicating a well-defined and narrowly distributed Na-Na hopping distance that closely matches the AIMD-derived migration length scales. In contrast, NTC exhibits broader and longer Na-Na separations centered around ~5.2 Å, reflecting less favorable and less uniform hopping geometries.

Analysis of the non-Na framework further reveals that NTSC possesses a robust network of loop-like cavities, as evidenced by one-dimensional Betti-number barcodes persisting continuously from ~3.6 to 5.2 Å. These cavities span length scales that overlap directly with the characteristic Na^+ hopping distances, providing a structurally and topologically compatible environment for multidimensional Na^+ diffusion. By comparison, the corresponding cavity network in NTC collapses beyond ~4.2 Å, indicating a fragmented framework with limited percolation pathways. As a result, Na^+ migration in NTC is more constrained and energetically hindered.

Collectively, the AIMD simulations and topological analyses reveal that NTSC combines short Na-Na hopping distances, softened Na-anion interactions, and a persistent cavity-rich framework across multiple length scales. These features directly reflect the experimentally observed mixed-anion coordination, Ta-centered oligomeric connectivity, and amorphous disorder, and together provide a mechanistic explanation for the low activation energy and superionic Na^+ transport observed in NTSC. This topology-informed understanding highlights how mixed-anion amorphization can be leveraged to engineer fast-ion conductors beyond the limitations of conventional crystalline halide electrolytes.

To further assess the practical viability of NTSC as a Na-ion solid-state electrolyte, all-solid-state sodium-ion batteries were assembled and evaluated at room temperature. Half-cells with the configuration Na_3Sn_4 | Na_3PS_4 | NTSC | $NaCrO_2$/NTSC/C were employed (Figure 4a). Owing to the intrinsic electrochemical instability of NTSC at low potentials, Na_3PS_4, which exhibits ionic conductivity of 0.21 mS/cm, was introduced to stabilize the interface with the Na_3Sn_4 anode (Figure S11).

Figure 4b shows the initial galvanostatic charge-discharge profiles of the NTSC-based cell recorded at 0.1 C within a voltage window of 1.88-3.98 V versus LiIn, corresponding to 2.4-3.4 V versus $Na_{15}Sn_4$. At room temperature, the cell delivers a high initial discharge capacity of 111.95 mAh/g with an initial Coulombic efficiency of 92.6% (Figure 4b), demonstrating good electrochemical reversibility. With increasing current density, reversible discharge capacities of 93.48, 51.25, and 21.78 mAh/g are achieved at 0.2, 0.5, and 1 C, respectively (Figure 4c). The noticeable capacity decay at higher C-rates, particularly beyond 0.5 C, is primarily attributed to the limited ionic conductivity of Na_3PS_4[11]. Long-term cycling performance was further evaluated at 0.2 C. As shown in Figure 4d, the cell exhibits excellent cycling stability, retaining 76.9% of its initial discharge capacity after 200 cycles with stable Coulombic efficiency. This sustained performance highlights the favorable electrochemical compatibility of NTSC with the $NaCrO_2$ cathode.

Overall, these results demonstrate that NTSC enables highly reversible Na^+ storage and robust long-term cycling stability in all-solid-state sodium-ion batteries at room temperature.

Conclusion

We report a new amorphous superionic Na-ion solid-state electrolyte, $TaCl_5$-0.5Na_2S (NTSC), synthesized via high-energy ball milling from $TaCl_5$ and Na_2S precursors. Owing to its mixed-anion amorphous framework, NTSC exhibits a high room-temperature ionic conductivity of 2.9 mS cm^{-1}. When implemented in all-solid-state sodium-ion batteries with the configuration Na_3Sn_4 | Na_3PS_4 | NTSC | $NaCrO_2$/NTSC/C, the electrolyte enables a high initial discharge capacity of 111.95 mAh/g, a Coulombic efficiency of 92.6%, and excellent cycling stability, retaining 76.9% of its capacity after 200 cycles at 0.2 C.

Comprehensive structural characterization reveals that NTSC consists of Ta-centered bi-polyhedral interconnected via corner-sharing sulfur atoms [$Ta_2Cl_{10}S$], forming a highly disordered yet structurally coherent amorphous network. This framework weakens Na^+-anion interactions and creates a flexible, disordered environment that supports fast Na^+ migration. Consistent with these experimental observations, *ab initio* molecular dynamics simulations identify continuous Na^+ diffusion pathways and a low migration barrier, confirming the intrinsic superionic nature of NTSC. Further topological analysis demonstrates that sulfur-induced lattice distortions shorten Na-Na hopping distances and generate

persistent, multidimensional transport cavities, providing a topology-level explanation for the experimentally observed low activation energy and high ionic conductivity.

Together, these results highlight how mixed-anion chemistry and amorphization can be synergistically exploited to overcome the transport limitations of conventional halide electrolytes. This work not only introduces a new class of high-performance amorphous Na-SSEs but also establishes clear structural and topological design principles for engineering next-generation solid electrolytes with enhanced ionic conductivity and improved electrochemical compatibility.

Experiment section

Materials synthesis

NTSC solid electrolytes: Na_2S (99.5%, sigma-Aldrich) and $TaCl_5$ (99.8%, sigma-Aldrich) were weighed to the stoichiometric molar ratio and mechanically mixed in a ZrO_2 container with ZrO_2 balls (diameter = 5 and 10 mm, 1:1, wt %) in a planetary ball mill (Fritsch, Pulverisette 7) at 500 rpm for 40 hours. The powder obtained was collected for further use.

Na_3PS_4 (NPS) solid electrolytes: SEs were synthesized by ball-milling a stoichiometric mixture of Na_2S and P_2S_5 in a ZrO_2 container with ZrO_2 balls (diameter =10 mm, ball to powder weight ratio=30:1) in a planetary ball mill (Retsch PM100) at 550 rpm for 3 h. The obtained powder was pelletized (at 150 MPa) and further annealed at 270 °C for 2 h.

Na-Sn alloy: Na and Sn with a stoichiometric molar ratio (15:4) were added in ball-milling jars in glovebox and further mechanically mixed for 4 h under 500 rpm. The obtained powder was collected for further use.

Preparation of cathode composites: cathode composite was obtained through mixing $NaCrO_2$, NTSC and C together with a weight ratio of 65:30:5 at 150 rpm for 2h.

Characterizations

XRD: The X-ray diffraction (XRD) measurements were performed on a Bruker Davinci 1 with a Cu Kα radiation (λ=1.54178 Å) at room temperature. The data were collected by scanning 1s per step with a step width of 0.02 from 10° to 80° (2θ). High-resolution X-ray data were refined using the Rietveld method (Bruker TOPAS V6 software). The background was modelled with a Chebyshev polynomic function of 5th order, and the fundamental parameter approach was chosen as the peak shape function.

SEM: The morphologies of solid electrolytes and cathode composites were characterized by a FEI Apreo emission scanning electron microscopy (SEM) equipped with energy dispersive spectroscopy (EDS).

DSC: Approximately 10 mg of the sample was sealed in an aluminum pan and heated under continuous nitrogen flow to prevent degradation. Measurements were conducted from 25 to 500 °C at a heating rate of 10 °C/min.

Raman: Raman tests were conducted by Renishaw RM-1000 spectrometer with a laser wavelength of 532 nm.

XPS: Chemical characterizations of the samples and the state of the surface were obtained with X-Ray Photoemission Spectroscopy (XPS). Core level spectra were measured using a monochromatized Al Kα (1486.6 eV) line with a hemispherical analyzer at NTNU XPS facilities and a Mg Kα (1253.6 eV) non-monochromatized light. Measurements were performed at room temperature and with chamber pressures

below 10^{-9} mbar. The calibration of the binding energy was done using C 1s and Au 4f reference peaks. The peaks fitting was optimized using a casa XPS software.

XAS: sulfur and chlorine *K-edge* XAS spectra were collected at the bending magnet ASTRA beamline at the SOLARIS National Synchrotron Radiation Center (Krakow, Poland). The measurements were performed in transmission and fluorescence modes at room temperature using an incident photon beam provided by a modified Lemonnier-type double-crystal monochromator equipped with Si(111) crystals. Energy calibration at the *S K-edge* was carried out using $ZnSO_4 \cdot 7H_2O$ (white-line position at 2481.4 eV), while calibration at the *Cl K-edge* was performed using KCl (white-line position at 2825.0 eV). The measurements were conducted using ionization chambers, with the ionization and sample chambers filled with pure N_2 at pressures of 25 torr and 27 torr, respectively. For the measurements, the powder samples were sealed between two sulfur-free and chlorine-free tapes in a glovebox under an argon atmosphere, forming a thin, uniform layer. The final spectra were obtained by merging at least three consecutive scans[17]. The sodium *K-edge* XAS spectra were collected in a fluorescence and total electron yield (TEY) modes at PIRX beamline at the SOLARIS[18]. The energy resolution was at the level of 200 meV. Tantalum L_3*-edge* were collected at BM31 beamline in ESRF with sealing BN-NTSC or BN-$TaCl_5$ mixture (80:20, wt%) (pellet shape) within aluminum laminate film. All spectra were processed using the Athena program from the Demeter software package.

xPDF: xPDF tests for $TaCl_5$, NTC and NTSC were conducted at BM31 beamline in ESRF with sealing samples in capillary.

Electrochemical measurements

Impedance spectroscopy: The Li-ion conductivity of solid electrolytes was measured by adding 0.15 g of solid electrolyte powder into a PEEK (polyether ether ketone) cell with a diameter of 10 mm and further pressed at 300 MPa. EIS measurements were carried out at 375 MPa and room temperature (25 °C, unless specified) in the frequency range of 10 to 7 MHz with 10 mV of applied sinus amplitude on VMP-300 potentiostat (BioLogic). The collected impedance data were analyzed and fitted using EC-LAB software based on the method of Randomize+simplex. To determine the individual contributions of the bulk (R_b) and grain boundary (R_{gb}) resistances, the Nyquist plots were fitted to an equivalent circuit model consisting of R1+Q2/R2.

Half-cell assembling: 40 mg of NPS was added in the PEEK cell with a diameter of 10 mm and pressed at 375 MPa; then, 40 mg NTSC powder was placed on the one side of the NPS pellet and pressed at the same pressure; the cathode composite was placed on the top of NTSC and pressed at 375 MPa; finally, 80 mg of Na-Sn alloy was homogeneously added on the other side of the NPS pellet and pressed at 200 MPa. The half-cells were tested at room temperature (25 °C) at 120 MPa pressure using Neware battery cycler.

Computational Methods

Density Functional Theory Calculations (DFT) and Structural Optimization: All first-principles calculations were performed within the framework of DFT using the Vienna Ab initio Simulation Package (VASP). The interaction between core and valence electrons was described by the projector augmented wave (PAW) method, and the exchange-correlation functional was treated using the Perdew-Burke-Ernzerhof (PBE) generalized gradient approximation.

To obtain highly accurate geometries and reliable bond lengths for subsequent dynamical and topological analyses, all structures were fully optimized using a high-precision setup. The plane-wave kinetic energy cutoff was set to 520 eV. The electronic self-consistent convergence criterion was 10^{-5} eV, and ionic relaxations were stopped when the residual forces on each atom were smaller than 0.005 eV/ Å.

Geometry optimizations were performed using the conjugate-gradient algorithm. A $3\times3\times1$ Monkhorst-Pack k-point mesh was employed for Brillouin zone sampling. The real-space projection approximation was disabled (LREAL=.FALSE.) and a finer FFT grid was used (ADDGRID=.TRUE.) to ensure numerical accuracy. Non-spherical contributions inside the PAW spheres were explicitly included (LASPH=.TRUE.), which is essential for systems containing the heavy Ta element. Symmetry was switched off (ISYM=0) to avoid artificial constraints on local structural distortions induced by S substitution.

Ab initio molecular dynamics simulations: Ab initio molecular dynamics (AIMD) simulations were performed on fully optimized structures to investigate Na^+ diffusion behavior. A 3 × 3 × 1 supercell was employed to minimize finite-size effects and enable sufficient Na^+ migration events. All simulations were conducted in the canonical (NVT) ensemble using a Nosé–Hoover thermostat with a time step of 0.5 fs. Each trajectory was propagated for 10,000 steps (5 ps) at elevated temperatures of 600, 800, 1000, and 1200 K to ensure adequate sampling of Na^+ hopping events. Brillouin-zone sampling was restricted to the Γ point of reducing computational cost.

A reduced plane-wave cutoff energy of 480 eV and a normal precision setting were adopted to balance numerical accuracy and efficiency. Gaussian smearing with a width of 0.05 eV was applied to facilitate electronic convergence, and the temperature was maintained constant throughout each simulation (TEBEG = TEEND).

Diffusion Coefficient and Ionic Conductivity: Na^+ mean square displacements (MSDs) were calculated from the AIMD trajectories, and diffusion coefficients were obtained using the Einstein relation:

$$\mathrm{D} = \lim_{t\to\infty} \frac{1}{6t} \langle |r(t) - r(0)|^2 \rangle ,$$

where $r(t)$denotes the position of a Na^+ ion at time t.

The temperature dependence of the diffusion coefficients was fitted using the Arrhenius equation:

$$D(T) = D_0 \exp\left(-\frac{E_a}{k_B T}\right).$$

The ionic conductivity was estimated using the Nernst-Einstein relation:

$$\sigma = \frac{nq^2 D}{k_B T},$$

where n is the number density of mobile Na ions, q is the elementary charge, k_B is the Boltzmann constant, and T is the temperature. The room-temperature ionic conductivity was obtained by extrapolating the Arrhenius fit to 300K.

Radial Distribution Function (RDF) Analysis: Radial distribution functions (RDFs) between Na-S and Na-Cl pairs were computed from the AIMD trajectories by time averaging over the production runs, to characterize the local chemical environment of Na ions in $TaCl_5$-0.5Na_2S and $NaTaCl_6$.

Topological Data Analysis and Persistent Homology: Persistent homology, a topological data analysis (TDA) approach, provides a rigorous framework for quantifying multiscale topological features in complex geometric data. In TDA, atomic configurations are represented using simplicial complexes composed of simplices, where a *k*-simplex is defined by *k* + 1 vertices (e.g., points, edges, triangles, and tetrahedra for *k* = 0-3). A filtration is constructed by generating a sequence of nested simplicial complexes with an increasing length scale parameter ε:

$$\emptyset \subseteq K(\epsilon_1) \subseteq K(\epsilon_2) \ldots \subseteq K(\epsilon_n),$$

At each scale, topological features such as connected components, loops, and cavities are quantified using homology. The number of independent *k*-dimensional features is given by the Betti number β_k. Persistent homology tracks the emergence (birth) and disappearance (death) of these features along the filtration. Features with long lifetimes are considered topologically robust, whereas short-lived features are typically associated with noise. The resulting multiscale information is visualized using persistence barcodes or persistence diagrams.

To probe topological characteristics relevant to Na^+ transport, persistent homology analysis was performed on two-point clouds derived from each structure: (i) the Na^+ sublattice and (ii) the non-Na framework comprising the Ta–Cl/S network. For a point set $X = \{x_i\} \subset \mathbb{R}^3$, Vietoris–Rips (VR) complexes $\mathrm{VR}(X, r)$were constructed by connecting points separated by distances smaller than a filtration parameter r, with higher-dimensional simplices added when all lower-dimensional faces were present. Increasing $r$generated a nested filtration:

$$\mathrm{VR}(X, r_1) \subseteq \mathrm{VR}(X, r_2) \subseteq \cdots \subseteq \mathrm{VR}(X, r_n), \qquad r_1 < r_2 < \cdots < r_n.$$

At each filtration scale, Betti numbers were computed, where $\beta_0$represents the number of connected components and $\beta_1$corresponds to independent loop-like features. The 0D persistence (β_0) of the Na^+ sublattice was used to extract characteristic Na–Na connectivity and hopping length scales, as the death

times reflect distances at which isolated Na sites become connected. In contrast, the 1D persistence (β_1) of the non-Na framework was analyzed to quantify the presence and stability of loop-like cavities that can accommodate and facilitate Na^+ migration. All persistent homology calculations were carried out using the Ripser package.

Na-ion migration pathways: Na^+ migration pathways were visualized by accumulating Na^+ trajectories from AIMD simulations and projecting them onto crystallographic planes. Regions with high probability density were rendered to identify continuous Na^+ diffusion channels.

Notes:

The authors declare no competing financial interest.

Acknowledgments

DR, and FJ gratefully acknowledge the financial support under the scope of the COMET program within the K2 Center "Integrated Computational Material, Process and Product Engineering (IC-MPPE)" (Project ASSESS P1.10). DR acknowledge financial support by the Austrian Federal Ministry for Digital and Economic Affairs, the National Foundation for Research, Technology and Development and the Christian Doppler Research Association (Christian Doppler Laboratory for Solid State Batteries). The Swiss Norwegian Beamline (SNBL@ESRF), ASTRA beamline and PRIX beamline at SOLARIS are acknowledged for providing of beamtime. The BM31 setup was funded by the Swiss National Science Foundation (grant 2021_18962) and the Research Council of Norway (grant 296087). The XAS measurements at the ASTRA beamline were supported by the Polish Ministry of Science and Higher Education under the project "Support for research and development with the use of research infrastructure of the National Synchrotron Radiation Centre SOLARIS" (contract no. 1/SOL/2021/2). The development of the ASTRA beamline at SOLARIS Centre was supported by the EU Horizon 2020 program (grant no. 952148-Sylinda). Financial support from the Research Council of Norway to NORTEM (grant 197405), National Natural Science Foundation of China (Grant No. 92472206), National Center for International Research of Power Batteries and Materials (No.2015B01015) and NorFab (grant 245963/F50) is acknowledged. We thank Halvor Helgeland and Hung Quoc Nguyen for providing $Na_{15}Sn_4$ anode and Na_3PS_4. We thank Zhan Zhaohuang for DSC measurement.

References

[1] X. Zhang, H. Qu, W. Yan, L. Yang, Y. Li, B.-L. Su, "Sodium-Based Dual-Ion Battery: From Materials to Mechanism" *Angewandte Chemie* **2025**, *137*, e202510566.

[2] S. Zhao, H. Che, S. Chen, H. Tao, J. Liao, X.-Z. Liao, Z.-F. Ma, "Research Progress on the Solid Electrolyte of Solid-State Sodium-Ion Batteries" *Electrochem. Energy Rev.* **2024**, *7*, 3.

[3] Y. Yang, S. Yang, X. Xue, X. Zhang, Q. Li, Y. Yao, X. Rui, H. Pan, Y. Yu, "Inorganic All-Solid-State Sodium Batteries: Electrolyte Designing and Interface Engineering" *Advanced Materials* **2024**, *36*, 2308332.

[4] Y. Li, X. Tang, Q. Li, Y.-X. Yin, L. Liu, J. Zhao, Y.-S. Hu, "Halide Solid-State Electrolytes for All-Solid-State Sodium Batteries: Progress and Perspectives" *ACS Energy Lett.* **2025**, *10*, 5520–5541.

[5] Z. Wei, L. F. Nazar, J. Janek, "Emerging Halide Solid Electrolytes for Sodium Solid-State Batteries: Structure, Conductivity, Paradigm of Applications" *Batteries & Supercaps* **2024**, *7*, e202400005.

[6] T. Zhao, A. N. Sobolev, R. Schlem, B. Helm, M. A. Kraft, W. G. Zeier, "Synthesis-Controlled Cation Solubility in Solid Sodium Ion Conductors Na2+xZr1–xInxCl6" *ACS Appl. Energy Mater.* **2023**, *6*, 4334–4341.

[7] C. Hunter, M. Ingram, "Na+-ion conducting glasses" *Solid State Ionics* **1984**, *14*, 31–40.

[8] N. Tanibata, K. Noi, A. Hayashi, M. Tatsumisago, "Preparation and characterization of highly sodium ion conducting $Na_3 PS_4$ –$Na_4 SiS_4$ solid electrolytes" *RSC Adv.* **2014**, *4*, 17120–17123.

[9] A. Hayashi, K. Noi, A. Sakuda, M. Tatsumisago, "Superionic glass-ceramic electrolytes for room-temperature rechargeable sodium batteries" *Nat Commun* **2012**, *3*, 856.

[10] Y. Hu, J. Fu, X. Lin, J. Xu, J. Luo, F. Zhao, Y. Liu, W. Li, J. T. Kim, H. Su, X. Hao, H. Ren, M. Yang, Y. Huang, X. Sun, "Superionic Amorphous NaTaCl6 Halide Electrolyte for Highly Reversible All- Solid-State Na-ion Batteries" *Matter* **2024**, *7*, 1018–1034.

[11] X. Lin, Y. Zhao, C. Wang, J. Luo, J. Fu, B. Xiao, Y. Gao, W. Li, S. Zhang, J. Xu, F. Yang, X. Hao, H. Duan, Y. Sun, J. Guo, Y. Huang, X. Sun, "A Dual Anion Chemistry-Based Superionic Glass Enabling Long-Cycling All-Solid-State Sodium-Ion Batteries" *Angew Chem Int Ed* **2024**, *63*, e202314181.

[12] X. Wang, S. Zhang, J. Yue, X. Wang, Y. Xu, Y. Gong, L. Zhou, C. Zhao, J. Liang, X. Zhu, H. Wu, X. Yan, B. Xiao, M. Li, C. Li, S. Wang, X. Sun, X. Li, "A new class of carbonate–oxychloride solid electrolytes for high-performance sodium-ion all-solid-state batteries" *Energy Environ. Sci.* **2025**, *18*, 9927–9938.

[13] J. Yue, F. Han, X. Fan, X. Zhu, Z. Ma, J. Yang, C. Wang, "High-Performance All-Inorganic Solid-State Sodium–Sulfur Battery" *ACS Nano* **2017**, *11*, 4885–4891.

[14] E. M. Lacinska, M. Furman, J. Binder, I. Lutsyk, P. J. Kowalczyk, R. Stepniewski, A. Wysmolek, "Raman Optical Activity of 1T-TaS_2" *Nano Lett.* **2022**, *22*, 2835–2842.

[15] S. Fan, S. Neal, C. Won, J. Kim, D. Sapkota, F. Huang, J. Yang, D. G. Mandrus, S.-W. Cheong, J. T. Haraldsen, J. L. Musfeldt, "Excitations of Intercalated Metal Monolayers in Transition Metal Dichalcogenides" *Nano Lett.* **2021**, *21*, 99–106.

[16] Z. L. Dong, Y. Gan, V. Martins, X. Wang, B. Fu, E. Jin, Y. Gao, Y. Hu, X. Lin, Y. Yuan, C. Turner, X. Pang, H. Abdolvand, Y. Huang, T. Sham, Y. Zhao, "Novel Sulfide-Chloride Solid-State Electrolytes with Tunable Anion Ratio for Highly Stable Solid-State Sodium-Ion Batteries" *Advanced Materials* **2025**, *37*, 2503107.

[17] B. Ravel, M. Newville, "ATHENA, ARTEMIS, HEPHAESTUS: data analysis for X-ray absorption spectroscopy using IFEFFIT" *J Synchrotron Rad* **2005**, *12*, 537–541.

[18] M. Zając, T. Giela, K. Freindl, K. Kollbek, J. Korecki, E. Madej, K. Pitala, A. Kozioł-Rachwał, M. Sikora, N. Spiridis, J. Stępień, A. Szkudlarek, M. Ślęzak, T. Ślęzak, D. Wilgocka-Ślęzak, "The first experimental results from the 04BM (PEEM/XAS) beamline at Solaris" *Nuclear Instruments and Methods in Physics Research Section B: Beam Interactions with Materials and Atoms* **2021**, *492*, 43–48.

Figures

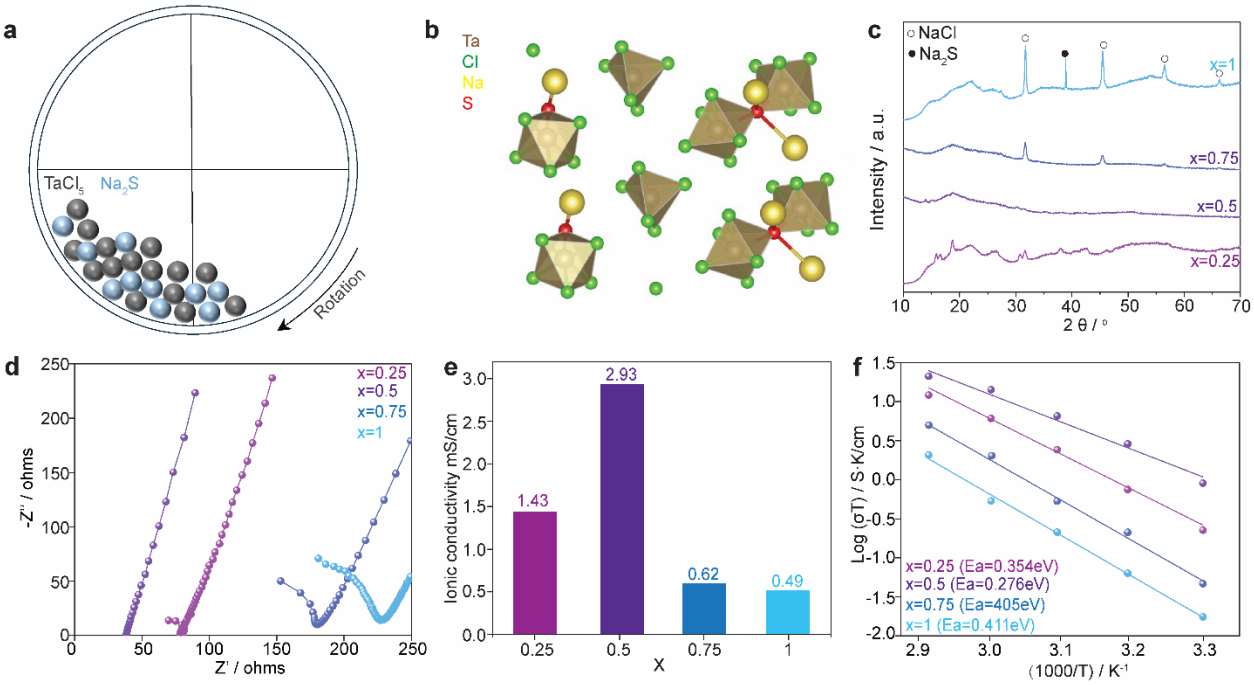

Figure 1. Synthesis and ionic transport properties of amorphous $TaCl_5$-xNa_2S solid electrolytes. (a) Schematic illustration of the high-energy ball-milling synthesis of $TaCl_5$-xNa_2S using $TaCl_5$ and Na_2S as precursors. (b) Structural model illustrating the local mixed-anion coordination environment in amorphous $TaCl_5$-0.5Na_2S. (c) X-ray diffraction (XRD) patterns of $TaCl_5$-xNa_2S (x = 0.25-1.0), highlighting the formation of a fully amorphous phase at x = 0.5. (d) Nyquist plots of $TaCl_5$-xNa_2S (x = 0.25-1.0) SEs and the corresponding calculated Na^+ ionic conductivities (e) at room-temperature as a function of Na_2S content, identifying $TaCl_5$-0.5Na_2S as the optimal composition. (f) Arrhenius plots of Na^+ conductivity for $TaCl_5$-xNa_2S solid electrolytes and their calculated values of activation energy.

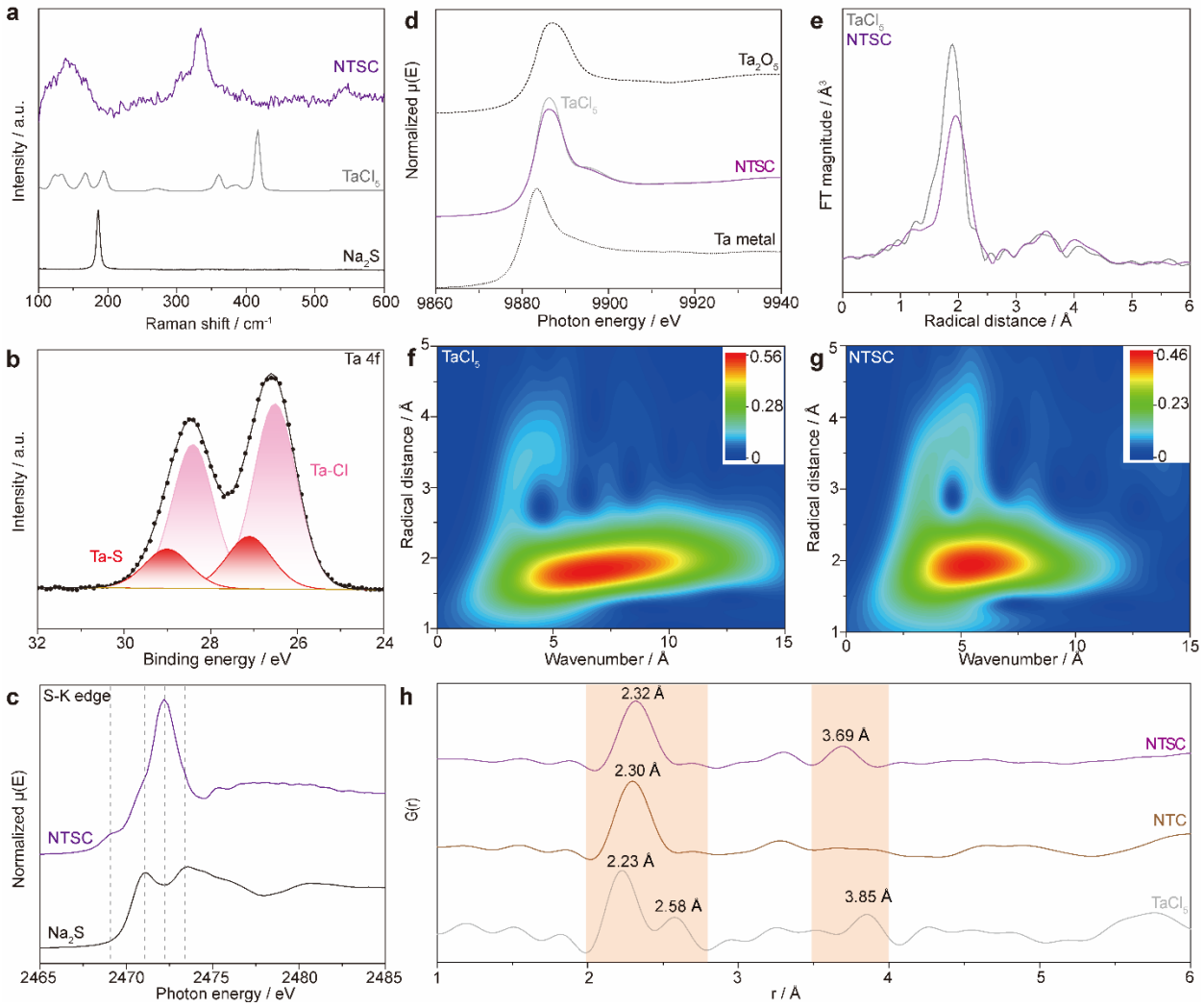

Figure 2. Structural characterization of the amorphous NTSC electrolyte. (a) Raman spectra of $TaCl_5$, Na_2S, and NTSC, showing the suppression and broadening of precursor vibrational modes upon amorphization. (b) Ta 4f X-ray photoelectron spectroscopy (XPS) spectrum of NTSC, revealing mixed sulfur coordination environments. (c) Normalized S *K-edge* X-ray absorption near-edge structure (XANES) spectra of Na_2S and NTSC, indicating preserved sulfur oxidation state and a largely unchanged Na^+ local chemical environment in the amorphous framework. (d) Normalized Ta *L_3-edge* X-ray absorption near-edge structure (XANES) spectra of $TaCl_5$ and NTSC. (e) Fourier-transformed (FT) curves at R space of $TaCl_5$ and NTSC. Wavelet-transformed extended X-ray absorption fine structure (WT-EXAFS) at the Ta *L_3-edge* for $TaCl_5$ (f) and NTSC (g), resolving nearest-neighbor Ta-S and Ta-Cl interactions and medium-range Ta-Ta correlations. (g) X-ray pair distribution function (xPDF) profiles of $TaCl_5$, $NaTaCl_6$ (NTC) and NTSC, highlighting the emergence of pronounced Ta-Ta correlations in NTSC consistent with oligomeric Ta-centered frameworks interconnected via corner-sharing sulfur atoms.

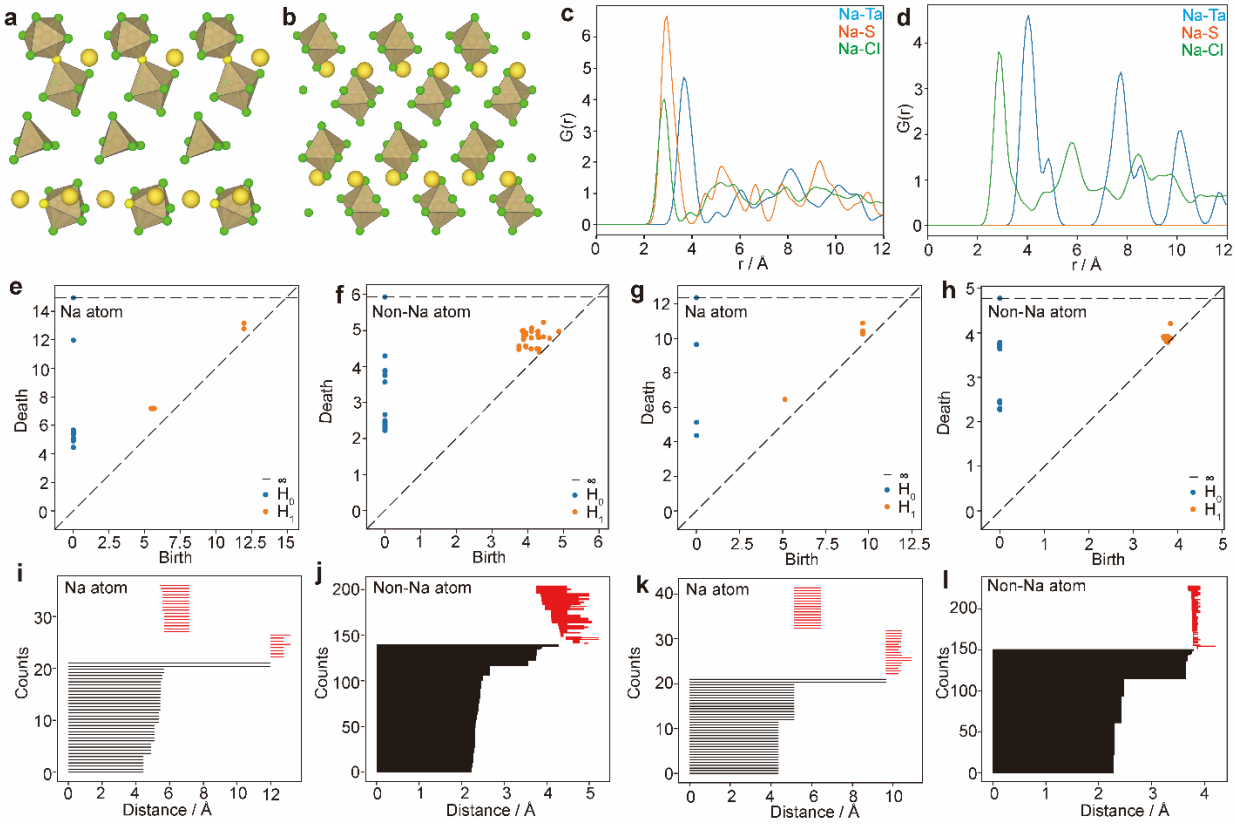

Figure 3. Atomistic origin of fast Na^+ transport in NTSC revealed by simulations and topological analysis. (a,b) Representative structural models of amorphous NTSC (a) and crystalline NTC (b), with highlighted pathways indicating potential Na^+ migration channels. (c,d) Radial distribution functions (RDFs) of NTSC (c) and NTC (d), showing shortened Na-Na distances and modified Na-anion correlations in NTSC arising from mixed-anion coordination. (e,h) Persistent homology analysis of NTSC (e,f) and NTC (g,h), shown separately for the Na-ion subnetwork (e,g) and the non-Na framework (f,h), illustrating differences in Na-Na hopping distances and framework connectivity. (i,l) Corresponding barcode representations, highlighting the presence of well-defined Na–Na hopping distances and a robust, cavity-rich framework in NTSC, in contrast to the more fragmented topology of NTC.

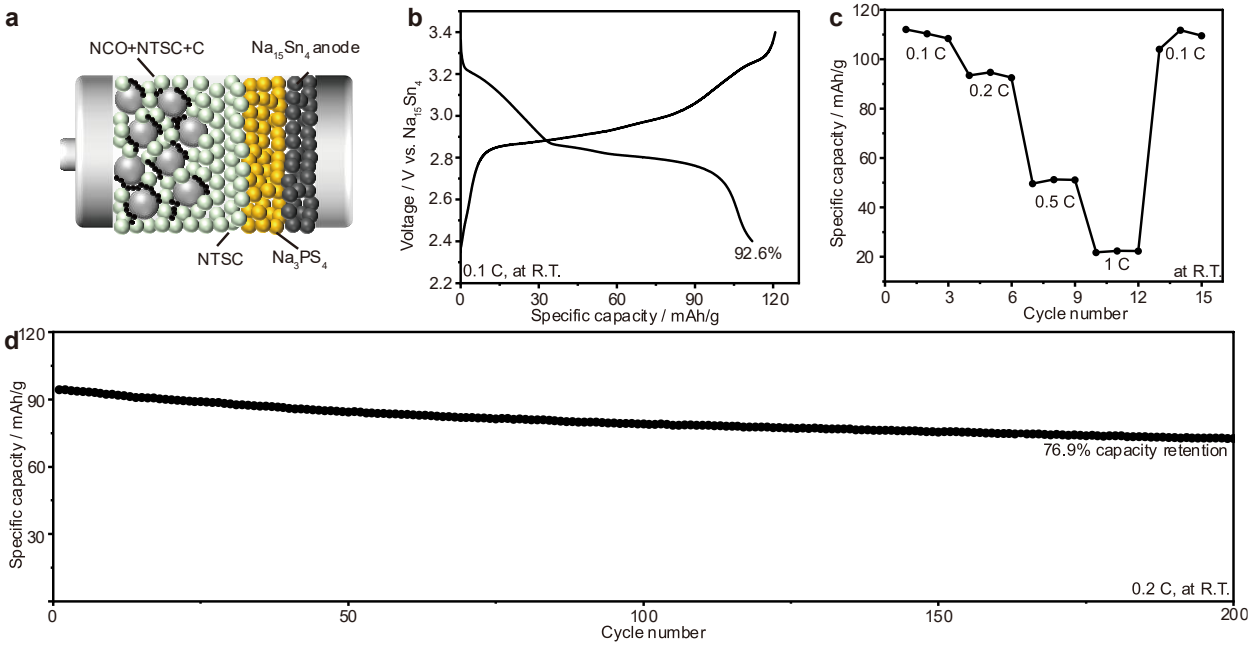

Figure 4. Electrochemical performance of NTSC-based all-solid-state sodium-ion batteries. (a) Schematic illustration of the NTSC-based solid-state battery configuration ($Na_{15}Sn_4$ | Na_3PS_4 | NTSC | $NaCrO_2$/NTSC/C). (b) Initial galvanostatic charge–discharge profiles recorded at 0.1 C and room temperature. (c) Rate performance of the NTSC-based cell at different current densities, demonstrating reversible Na^+ storage. (d) Long-term cycling performance measured at 0.2 C, showing stable capacity retention over 200 cycles at room temperature.